Center for Turbulence Research
Proceedings of the Summer Program 2018

Reconstructing channel turbulence from wall observations

By M. P. Encinar†, A. Lozano-Durán AND J. Jiménez†

The reconstruction of the flow field in a turbulent channel from wall observations is studied. Motivated by the exact relation between the pressure and the second invariant, Π, of the velocity gradient tensor, it is found that Π can be reconstructed in the viscous layer to good accuracy from measurements of the pressure and of the two shears at the wall, but that the optimum technique is linear stochastic estimation, rather than the exact equation. The reconstruction substantially degrades beyond $y^+ \approx 100$, but only for the smallest scales. Beyond that height, the larger Π structures can still be observed from the wall. They share many characteristics with the attached vortex clusters studied in previous works, but not with individual vortices. All scales are reconstructed within the buffer layer, but only large attached ones farther from the wall.

1. Introduction

Control of wall-bounded turbulence is a classic goal of turbulence research, whether to decrease or increase wall friction, reduce noise or other applications. There is a well-developed theory for the optimal control of linear systems, and, although turbulence is nonlinear, there is extensive evidence that a substantial fraction of the dynamics of shear-driven flows can be linearized (Jiménez 2013). This has led to heuristic and theoretical active control schemes that manipulate friction in turbulent channels at moderate Reynolds numbers, at least in simulations (Choi *et al.* 1994; Farrell & Ioannou 1996), but they are not free from problems and ambiguities.

The first one has to do with the scales involved. Most of the dissipation in wall-bounded flows is contained within or below the logarithmic layer, suggesting that any effective control has to act near the wall. Most schemes have targeted the buffer layer, which is the site of the strongest shear, but technological considerations suggest that practical applications should mostly center on the logarithmic layer. Thus, for a flow of thickness h and Reynolds number $h^+ = u_\tau h/\nu$, where the '+' superscript denotes wall units based on the friction velocity u_τ and the kinematic viscosity ν, the sizes and passing times of the structures in the buffer layer decrease proportionally to h^+ when expressed in outer units. On the contrary, those in the logarithmic layer, where the distance, y, from the wall is a fixed fraction of h, scale independently of the Reynolds number. For example, in a pipe with $h \approx 1$ m and bulk velocity $U \approx 1$ m/s ($h^+ \approx 10^5$), the buffer-layer scales are $\Delta x \approx 1$ mm and $\Delta t \approx 0.1$ ms, but those at $y/h \approx 0.1$ are $\Delta x \approx 20$ cm and $\Delta t \approx 0.2$ s. Similar differences apply to the flow over airplane wings.

However, moving away from the wall is not without cost. Figure 1 presents the fraction of the total dissipation above a given level, and shows that the maximum fraction that could potentially be saved by removing all the dissipation between $y/h = 0.01$ and 0.2 in the example above is approximately 25%. Decreasing the lower limit increases the

† School of Aeronautics, Universidad Politécnica de Madrid, Spain

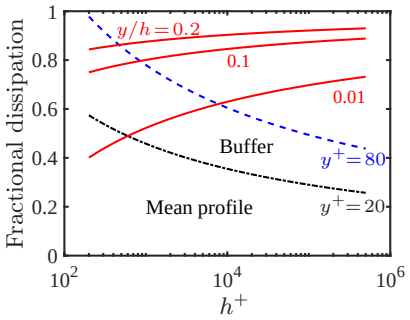

FIGURE 1. Fraction of the total energy dissipation below a given distance from the wall, as a function of the Reynolds number. The solid lines are three levels within the logarithmic layer (Jiménez 2018).

potential gain at the cost of smaller length and time scales. Raising the upper limit is less effective.

The second problem is that most active control schemes assume knowledge of the flow at wall distances of the order of the size of the structures to be controlled. Typically, the assumption is that the flow is fully known, as in direct numerical simulation (DNS), or that at least a two-dimensional section of some variables is available, as in particle image velocimetry (PIV). Unfortunately, most practical observations are limited to the wall, and the only accessible variables are the pressure and the two shears. This problem is specially acute when targeting the logarithmic layer, which is relatively far from the wall and separated from it by the very active buffer layer.

A related question is which part of the outer flow is effective in generating pressure fluctuations at the wall, which are of interest in acoustics and structural loading. Wall pressure can be computed exactly if the flow is fully known, as in DNS. But lower-fidelity large-eddy simulations (LES) computations only determine the outer flow approximately, and the question is which level of detail is required to predict wall pressure to a given accuracy.

This report addresses the second question first, and only then addresses the problem of estimating the state of the flow at interior points from measurements at the wall. In both cases, we try to use the fact that pressure satisfies a Poisson equation whose right-hand side is the object to be estimated. This differs from methods exclusively based on statistical correlations, which only determine the most probable reconstruction from a given observation. We will see that we eventually have to use statistical information to make our results physically plausible, but the use of two quantities linked by an equation at least guarantees that the observations are fully explained by the reconstruction. In a sense, equation-based approaches provide an upper bound for the performance of statistical ones, and give them a physical interpretation. The problem of determining the effectiveness of the right-hand side will turn out to reduce to a projection on an effective subspace, while that of optimal estimation can be understood as an extreme case of data assimilation (Rawlins *et al.* 2007).

2. Numerical data sets

We use data from DNSs of turbulent pressure-driven channels of half-width h in doubly periodic boxes of wall-parallel dimensions $L_x \times L_z$. The streamwise, wall-normal, and

Case	h^+	L_x	L_z	Reference
M950	932	2π	π	Lozano-Durán & Jiménez (2014)
W1900	1840	$\pi/2$	$\pi/4$	Flores & Jiménez (2010)

TABLE 1. Summary of the simulations used for data.

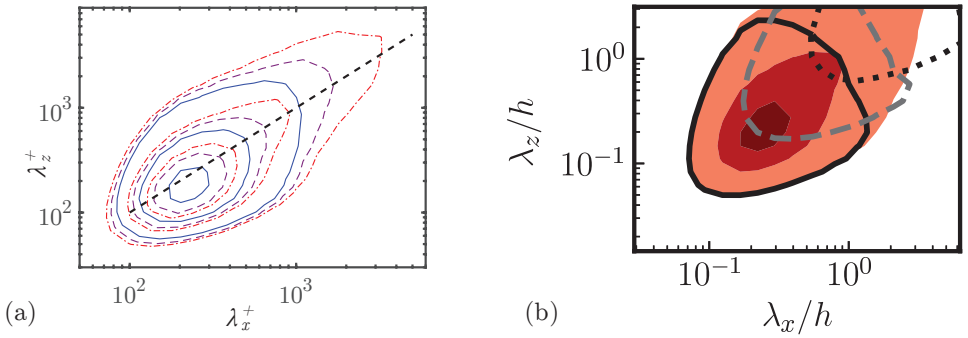

FIGURE 2. (a) Premultiplied pressure spectra at $y^+ = 5$. Contours are $k_x k_z E_{pp}^+ = (0.25, 0.50, 0.75)$, and the dashed diagonal is $\lambda_x = \lambda_z$. Large-box channels at: solid, $h^+ = 550$; dashed, 934; dash-dotted, 2000. Various sources. (b) Shaded contours are the pressure spectrum at the wall. Contours contain 10%, 50%, and 90% of the spectral mass, M950. solid, contribution from Eq. (7) below $y^+ = 60$; dashed, $60 < y^+ < 200$; dotted, $y^+ > 200$. Contours contain 63%, 18%, and 4% of the total pressure, and 80%, 38%, and 31% of the pressure in their spectral region.

spanwise directions are x, y and z, respectively. Their corresponding velocity components are u, v and w, and the vorticities are ω_i. Unless otherwise stated, repeated indices imply summation over the range $x \dots z$. Lowercase symbols represent fluctuating quantities with respect to ensemble averages, and primes denote root-mean-square (r.m.s.) fluctuation intensities.

The focus on the logarithmic layer requires the use of channels at reasonably high Reynolds numbers, $h^+ \gtrsim 1000$, but not necessarily of very large boxes. The two direct simulations used in the paper are summarized in Table 1. Channel M950 is a medium-size box in which turbulence should be healthy across the full domain (Lozano-Durán & Jiménez 2014), while W1900 is a smaller box for which data can only be trusted below $y \approx 0.25h$ (Flores & Jiménez 2010). Both cases therefore include healthy buffer and logarithmic layers. More details are found in the original publications.

3. Theoretical background

The pressure satisfies the Poisson equation

$$\nabla^2 p = 2\Pi, \tag{1}$$

where $\Pi = (\omega_i\omega_i - 2S_{ij}S_{ij})/4 = \partial_i u_j \partial_j u_i/2$ is the second invariant of the velocity gradient, and $S_{ij} = (\partial_i u_j + \partial_j u_i)/2$ is the rate-of-strain tensor. The pressure satisfies boundary conditions at both walls

$$\partial_y p = \nu \partial_{yy} v = \nu(\partial_x \omega_z - \partial_z \omega_x), \tag{2}$$

where the last equality follows from continuity and impenetrability.

Expanding in Fourier series along (x, z), and denoting Fourier coefficients by carats, Eq. (1) becomes

$$(\partial_{yy} - k^2)\widehat{p} = 2\widehat{\Pi}, \tag{3}$$

where $k^2 = k_x^2 + k_z^2$ is the wavenumber magnitude. Following Kim (1989), $\widehat{p}$ can be expressed as the sum of an "inertial" component, $\widehat{p}_\Pi$, satisfying Eq. (3) with homogeneous Neumann boundary conditions, and a "Stokes" contribution,

$$\widehat{p}_S = \left[-\partial_y\widehat{p}(0)\cosh k(2h-y) + \partial_y\widehat{p}(2h)\cosh ky\right]/k\sinh(2kh), \tag{4}$$

which satisfies Laplace's equation with boundary conditions, Eq. (2). The inertial pressure can be obtained from $\widehat{\Pi}$ by inverting Eq. (3) as

$$\widehat{p}_\Pi(y) = \int_0^{2h} \widehat{\Pi}(\zeta)G(y,\zeta)\,\mathrm{d}\zeta, \tag{5}$$

where the Green's function is

$$G(y,\zeta) = \begin{cases} -2\cosh k(2h-\zeta)\cosh ky/k\sinh 2kh, & \text{if} \quad y \le \zeta, \\ -2\cosh k\zeta\cosh k(2h-y)/k\sinh 2kh, & \text{otherwise.} \end{cases} \tag{6}$$

Note that, if the pressure and the two shears, $\partial_y u$ and $\partial_y w$, can be measured at both walls, the Stokes pressure follows from Eq. (2) and Eq. (4), and the inertial wall pressure, $\widehat{p}_{\Pi w} = \widehat{p}_w - \widehat{p}_{Sw}$, is observable. Note also that, except for very large structures in which $kh \ll 1$, the Stokes pressure is essentially determined locally by the boundary condition at each wall, and is small everywhere. In what follows, we suppress the subindex 'Π' when referring to the inertial pressure, but the results in Section 4 are corrected for the Stokes component. A preliminary analysis of these equations is presented by Jiménez & Hoyas (2008). Defining wavelengths as $\lambda_i = 2\pi/k_i$, the location of the core of the pressure spectrum away from the wall is approximately equilateral, $\lambda_x \approx \lambda_z \approx 3y$, and the intensity scales in wall units, $p(y/h) \sim u_\tau^2$.

Particularizing Eqs. (5)–(6) at the lower wall,

$$\widehat{p}_w = \int_0^{2h} \widehat{\Pi}(\zeta)G(0,\zeta)\,\mathrm{d}\zeta = \frac{-2}{k\sinh 2kh}\int_0^{2h} \widehat{\Pi}(\zeta)\cosh k(2h-\zeta)\,\mathrm{d}\zeta. \tag{7}$$

Near the wall, Figure 2(a) shows that the wavelengths of the spectrum scale well in wall units, suggesting that most of the pressure at the wall is due to flow structures in the buffer layer. But there is a substantial large-scale tail that lengthens with increasing Reynolds number, and therefore presumably originates farther into the flow. This is confirmed by Figure 2(b), which displays the contribution to the spectrum from different height intervals in the integral Eq. (7).

From the point of view of flow reconstruction, it is clear that the function $\widehat{\Pi}(y)$ cannot be fully characterized by the single number $\widehat{p}_w$, and that some kind of projection is required. There is a relatively well developed theory for linear optimal "state observers" in control theory (Sontag 1998), whose key result is that an observer can only be built for observable quantities. In the present context, this means that $\widehat{\Pi}$ should have a measurable effect at the wall to be reconstructible, but the exponential decay of the kernel in Eq. (7) suggests that this is not the case for many Π structures. Small eddies with $kh \gg 1$, whose Green's function decays fast with ky, are not observable and cannot be reconstructed far from the wall. We will see below that larger structures can.

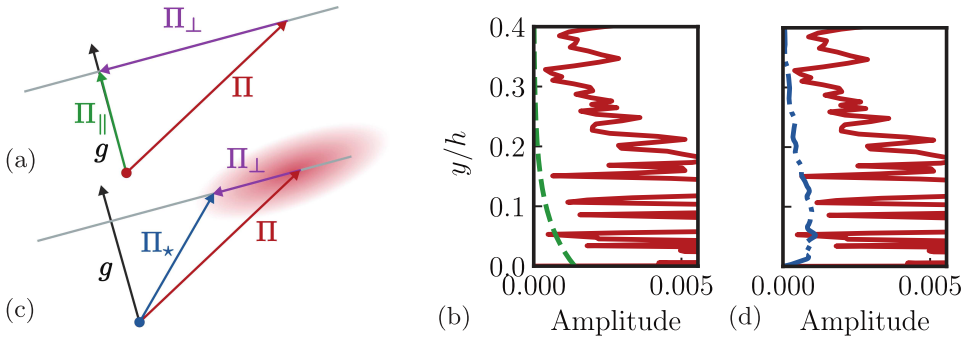

FIGURE 3. (a) Sketch of the pressure-generating subspace, with the orthogonal projection of Π on the Green's function. (b) Optimal reconstruction of Π based on the wall pressure. Solid line, Full $\widehat{\Pi}$; dashed line, minimum-norm orthogonal reconstruction, $\widehat{\Pi}_\parallel$; M950, $\lambda_x/h = 0.7, \lambda_z/h = 0.78$. (c) As in (a), emphasizing the known probability distribution of Π. (d) As in (b), for the minimum-error reconstruction. Solid line, $\widehat{\Pi}$; dash-dotted line, $\widehat{\Pi}_*$.

If we represent discretized functions of y as vectors, such as $\boldsymbol{g} \equiv G(0, y)$ and $\boldsymbol{\Pi} \equiv \widehat{\Pi}(y)$, Eq. (7) can be written as a matrix product,

$$\widehat{p}_w = \boldsymbol{g}^* \boldsymbol{\Pi}, \tag{8}$$

where the asterisk denotes Hermitian transpose. In practice, Eq. (8) has to incorporate the integration weights, as explained by Moin & Moser (1989). The situation is sketched in Figure 3(a). For a given $\widehat{p}_w$, Eq. (8) implies that $\boldsymbol{\Pi}$ lies in a hyperplane normal to $\boldsymbol{g}$, which is parallel to the null-space of the inner product. Any component in this subspace $\boldsymbol{\Pi}_\perp$, such that $\boldsymbol{g}^* \boldsymbol{\Pi}_\perp = 0$, does not contribute to the wall pressure. There are two optimization problems to be considered. The first one concerns which is the smallest $\boldsymbol{\Pi} = \boldsymbol{q}$ that generates a given $\widehat{p}_w$, and is equivalent to minimizing

$$\boldsymbol{q}^* \boldsymbol{q}, \quad \text{given} \quad \boldsymbol{g}^* \boldsymbol{q} = \boldsymbol{g}^* \boldsymbol{\Pi} = \widehat{p}_w. \tag{9}$$

The second one is to minimize the error between the predicted and observed $\boldsymbol{\Pi}$,

$$(\boldsymbol{\Pi}^* - \boldsymbol{q}^*)(\boldsymbol{\Pi} - \boldsymbol{q}), \quad \text{given} \quad \boldsymbol{g}^* \boldsymbol{q} = \boldsymbol{g}^* \boldsymbol{\Pi} = \widehat{p}_w. \tag{10}$$

For any given flow field, the answer to the second problem is trivially $\boldsymbol{q} = \boldsymbol{\Pi}$, with zero error, while the answer to the first one is the orthogonal projection of $\boldsymbol{\Pi}$ over $\boldsymbol{g}$,

$$\boldsymbol{\Pi}_\parallel = (\boldsymbol{g}^* \boldsymbol{\Pi}) \boldsymbol{g} / |\boldsymbol{g}|^2 = \widehat{p}_w \boldsymbol{g} / |\boldsymbol{g}|^2, \tag{11}$$

where $|\boldsymbol{g}|^2 = \boldsymbol{g}^* \boldsymbol{g}$. An example of $|\boldsymbol{\Pi}|$ and $|\boldsymbol{\Pi}_\parallel|$ for a particular Fourier mode and snapshot of channel M950 is given by the solid and dashed lines in Figure 3(b), illustrating that the optimum projection has the expected exponential form of the Green's function, but that most of $\boldsymbol{\Pi}$ is not contained in the projection.

Unfortunately, Eq. (11) is physically unrealistic because $\widehat{\Pi}$ has to satisfy constraints that are not taken into account by the above procedure. For example, it follows from incompressibility and from the no-slip velocity condition that $\widehat{\Pi} = 0$ at both walls, which is not true for the Green's function. In essence, Eq. (11) is a property of Poisson's equation, otherwise unrelated to the flow in a channel. On the other hand, it is the optimal solution of Eq. (8), and any other $\boldsymbol{\Pi}$, even if motivated by physical considerations, contains essentially arbitrary components which are unrelated to the pressure at the wall.

The simplest way to incorporate the properties of $\widehat{\Pi}$ into Eqs. (9)–(10) is to apply

the optimization to an ensemble average of flows, rather than to individual snapshots. Consider the reconstruction $\boldsymbol{q} \sim \boldsymbol{\phi}$, where $\boldsymbol{\phi}$ is a vector normalized as

$$\boldsymbol{g}^* \boldsymbol{\phi} = 1, \tag{12}$$

constant across snapshots. The condition that $\boldsymbol{q}$ reconstructs the correct pressure is

$$\boldsymbol{q} = \widehat{p}_w \boldsymbol{\phi}. \tag{13}$$

It is easy to check that this statistical modification has no effect on Eq. (9), whose solution is still the orthogonal projection, Eq. (11), but Eq. (10) contains $\boldsymbol{\Pi}$ explicitly, and the effect of incorporating its statistics is not trivial. The quantity to be minimized is

$$\langle (\boldsymbol{\Pi} - \widehat{p}_w \boldsymbol{\phi})^* (\boldsymbol{\Pi} - \widehat{p}_w \boldsymbol{\phi}) \rangle + \mu (1 - \boldsymbol{\phi}^* \boldsymbol{g}) + \ldots, \tag{14}$$

where $\langle \cdot \rangle$ is the ensemble average, the trailing dots represent terms that do not involve $\boldsymbol{\phi}^*$, and μ is the Lagrange multiplier that enforces Eq. (12). Differentiation with respect to $\boldsymbol{\phi}^*$ leads, after some algebra, to $\mu = 0$ and to the reconstruction

$$\boldsymbol{\Pi}_* = \widehat{p}_w \langle \widehat{p}_w^* \boldsymbol{\Pi} \rangle / \langle |\widehat{p}_w|^2 \rangle, \tag{15}$$

where the projector $\boldsymbol{\phi} = \langle \widehat{p}_w^* \boldsymbol{\Pi} \rangle / \langle |\widehat{p}_w|^2 \rangle$ plays the role of $\boldsymbol{g}//|\boldsymbol{g}|^2$ in Eq. (11). Some reflection reveals that $\boldsymbol{\phi}$ is an approximation to the direction of the mean value of the distribution of $\boldsymbol{\Pi}$ in function space. The only statistical object that needs to be compiled in Eq. (15) is the two-point correlation matrix $\boldsymbol{C} = \langle \boldsymbol{\Pi}\, \boldsymbol{\Pi}^* \rangle \equiv \langle \widehat{\Pi}(\zeta) \widehat{\Pi}^*(\zeta') \rangle$, because Eq. (8) implies that all the second-order statistics of $\widehat{p}_w$ can be derived by contracting $\boldsymbol{g}$ with $\boldsymbol{C}$. For example, $\langle \widehat{p}_w \boldsymbol{\Pi}^* \rangle = \boldsymbol{g}^* \boldsymbol{C}$, and $\langle |\widehat{p}_w|^2 \rangle = \boldsymbol{g}^* \boldsymbol{C} \boldsymbol{g}$.

Eq. (15) is a variant of linear stochastic estimation (LSE, Adrian 1994), which uses the joint statistics of a series of observed events, $\widehat{p}_w$, and unknowns $\widehat{\Pi}(y)$ to be estimated, to compute the linear operator minimizing the average error. In contraposition to Eq. (11), only statistical information is included in Eq. (15), which does not involve the Green's function $\boldsymbol{g}$, and is essentially independent of the physics in Eq. (1).

LSE has often been used on turbulent flow, but usually to derive mean flow behavior conditioned to particular events, or a local Taylor expansion for the velocities (Adrian 1994). An early attempt to estimate the instantaneous buffer-layer vortices from wall shear was made by Kravchenko *et al.* (1993), but we know of few other cases in which it has been used as a real-time flow estimator. As it is used here, there is no implication that $\widehat{\Pi}(y)$ can be locally expanded as a Taylor series of position. The assumption is that the perturbations of $\widehat{\Pi}$ are linearly related to the perturbations of $\widehat{p}_w$.

An example of this reconstruction for the case in Figure 3(b) is shown in Figure 3(d). It agrees better than $\boldsymbol{\Pi}_{\parallel}$ with the known statistical behavior of $\widehat{\Pi}$, including vanishing at the wall, but it is still a small fraction of the original $\widehat{\Pi}$. Most of the right-hand side of Eq. (3) is not observable from the wall.

4. Results

Wall-parallel two-dimensional spectra of Π are shown as line contours in Figure 4. They are approximately equilateral, except very near the wall, peaking at some multiple of the local Kolmogorov scale, $\lambda_i \approx 25\eta$. The same is true for the vorticities and for most of the velocity gradients (Jiménez 2018), and it is known that Π, enstrophy, and the discriminant of the velocity gradient are approximately equivalent representations of vortices (Chakraborty *et al.* 2005). The shaded contours in the figure are the fraction of

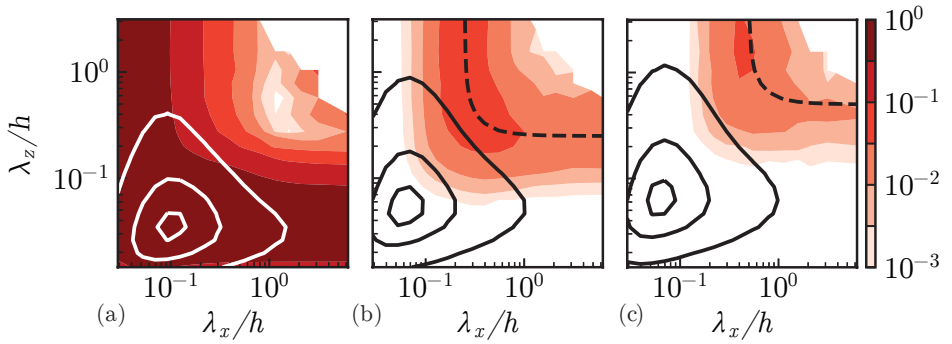

FIGURE 4. Line contours are the premultiplied spectrum of $\widehat{\Pi}$ for M950, with contours containing 90%, 50%, and 10% of the spectral mass at each height. Shaded contours are the fraction of $|\widehat{\Pi}|^2$ contained in the reconstruction in Eq. (15), with the color bar at right. Only wavenumbers for which $|\widehat{\Pi}|^2$ is above 10^{-3} of its maximum are included. (a) $y^+ = 9$. (b) $y^+ = 60$. The dashed line is $2\pi/kh = 0.25$. (c) $y^+ = 111$, and $2\pi/kh = 0.5$.

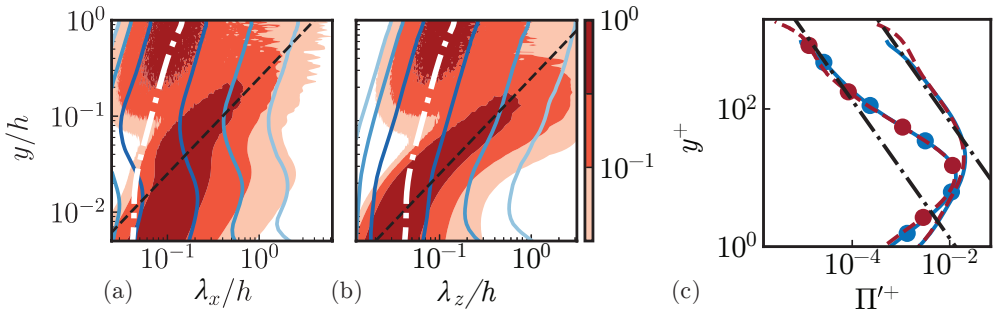

FIGURE 5. One-dimensional spectra of Π (lines) and its reconstruction (shaded), normalized to unit spectral mass at each height. In both cases, the contours are (0.032, 0.1, 0.32). ---- , $\lambda_i = 4y$; —·— , $\lambda_i = 25\eta$, where $\eta = \nu^{3/4}\varepsilon^{-1/4}$ is the Kolmogorov viscous length computed from the kinetic-energy dissipation ε. (a) As a function of the streamwise wavelength. (b) Spanwise. (c) R.m.s. fluctuation intensities for the true Π (without symbols), and for the reconstructed Π_* (symbols). ——— , M950; ---- , W1900. The two diagonals are $\Pi'^+ = 5/y^+$, and $0.1/y^+$.

the spectrum of Π reconstructed by Eq. (15). Figure 4(a) shows that the reconstruction is essentially exact within the viscous layer ($y^+ = 9$), at least with regard to the magnitude of Π, while Figure 4(b,c) shows that the reconstructible wavelengths are restricted to larger scales ($\lambda = 2\pi/k \approx 4y$), as y moves into the outer buffer and logarithmic layers. Modes where $|\widehat{\Pi}|^2 < 10^{-3}|\widehat{\Pi}|^2_{max}$, such as the largest scales, have been masked for clarity.

The evolution of the reconstruction with y is further analyzed in Figure 5(a,b), which shows the spectra of the observed and reconstructed Π as a function of the wavelengths and of y. It is interesting that, whereas the spectrum of Π tracks the Kolmogorov scales, as it does for the vorticity, that of Π_* peaks at $\lambda \approx 4y$, which is characteristic of the energy-containing eddies. Del Álamo *et al.* (2006) studied wall-attached clusters of vortices in channels. They showed that they are distinct from individual vortices, that their size grows linearly with y, and that clusters are associated with strong wall-normal velocities. Lozano-Durán *et al.* (2012) and Dong *et al.* (2017) later showed that vortex clusters are part of the sweep-ejection pairs responsible for a large fraction of the Reynolds stresses. Eq. (7) shows that the associated wavelengths are also responsible for the pressure fluc-

tuations at the wall. All these observations suggest that the eddies of the reconstructed Π are identical to the vortex clusters, as further shown in Section 4.1.

Figure 5(c) displays profiles of the r.m.s. intensities of Π and Π_*, and includes the two Reynolds numbers in Table 1. Dimensional considerations imply that $\Pi' \sim u_\tau^3/y$ in the scale-free logarithmic layer. The figure shows that this is true: Π' scales in wall units in the buffer layer, and the collapse extends into the logarithmic layer. Interestingly, the same applies to Π'_*. The two quantities approximately agree below $y^+ \approx 10$, beyond which Π'_* decays, recovering the $1/y$ trend above $y^+ \approx 100$. Comparison with the spectra in Figure 4 shows that the near-wall peak corresponds to eddies at buffer-layer scales, while the outer logarithmic trend corresponds to larger structures. Both del Álamo *et al.* (2006) and Lozano-Durán *et al.* (2012) found that vortex clusters are predominantly present near the wall, but that there is a population of self-similar Π structures that extends into the logarithmic layer. They cover a fraction of the wall-parallel area approximately independent of y. Del Álamo *et al.* (2006) justified this on the grounds of the percolation analysis used to determine the threshold that defines the clusters, but the proportionality in Figure 5(c) between the intensities of the observed and reconstructed Π, which use no threshold, suggests that it is a self-similarity property of the structures themselves.

4.1. *Three-dimensional reconstructions*

More information on the geometry of Π is provided by the investigation of the three-dimensional regions where Π or Π'_* are particularly intense. We focus on points satisfying

$$\Pi(x,y,z) > \alpha \Pi'(y), \tag{16}$$

$$\Pi_*(x,y,z) > \alpha_* \Pi'_*(y), \tag{17}$$

where $\alpha = 1.25$ and $\alpha_* = 1.75$ are thresholds selected by a percolation analysis as done by Moisy & Jiménez (2004), and Π and Π_* structures are defined as connected point sets satisfying Eqs. (16)–(17), respectively. Connectivity is defined in terms of the six orthogonal neighbors in the Cartesian DNS mesh. We have confirmed that the conclusions below remain valid for values of α and α_* that are half and double of those discussed below.

The size of individual structures is defined by the streamwise (l_x), wall-normal ($l_y = y_{max} - y_{min}$), and spanwise (l_z) lengths of their grid-aligned bounding box, where y_{min} and y_{max} are the minimum and maximum distance of each object to the closest wall, respectively. Following del Álamo *et al.* (2006), Π- and Π_*-structures are classified as wall-attached when $y^+_{min} < 20$ from the bottom wall, and as wall-detached otherwise. We do not consider structures attached to the top wall, because the reconstruction only uses information from $y = 0$.

Figure 6(a) contains the joint probability density function (p.d.f.) of the minimum and maximum wall distances of the structures. Both Π and Π_* structures are organized into wall-attached and wall-detached families. The former are contained in the narrow vertical band for $y^+_{min} < 20$, and the latter in the wider strip above the diagonal. Interestingly, the band for detached objects is narrower for Π_* structures, which tend to be smaller in the wall-normal direction. The streamwise and spanwise sizes of individual structures are quantified in Figure 6(b). The populations of Π and Π_* structures exhibit similar sizes, although the distribution of the reconstructed structures is biased towards smaller sizes, consistent with the lack of large detached structures reported above.

A better insight into the representation of true structures by the reconstructed field follows from the correlation between Π boxes (the bounding box of a Π structure) and

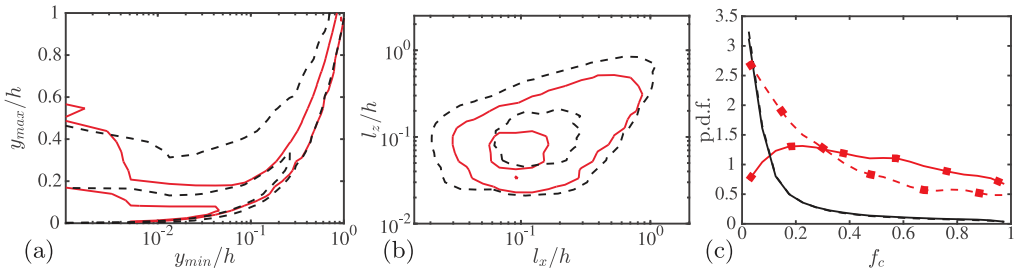

FIGURE 6. (a) Joint p.d.f. of the maximum and minimum wall distances of the identified Π and Π_* structures, $p(y_{min}, y_{max})$. Contours contain 98% and 50% of the probability. (b) Joint p.d.f. of the logarithms of the streamwise and spanwise sizes of Π and Π_* structures, $p(l_x/h, l_z/h)$. (c) P.d.f. of the intersected fraction of box-volume of Π boxes with Π_* boxes. Lines with and without squares are for wall-attached and wall-detached structures, respectively (the p.d.f. for detached structures is divided by two). Solid lines are the p.d.f. Dashed lines are computed for Π boxes with Π_* boxes at uncorrelated times. Note that the solid and dashed lines are indistinguishable for detached structures.

Π_*-boxes. For each Π box of volume V_b, we select the spatially intersecting Π_*-box with highest overlap V_i, and the correlation fraction between Π and Π_* boxes is defined as $f_c = V_i/V_b$. To quantify the amount of random overlap between structures, the calculation is repeated for Π and Π_* boxes from different uncorrelated times.

Figure 6(c) shows that there is a non-trivial overlap between wall-attached Π and Π_* boxes, while there is no significant correlation between the detached Π and Π_* families. The result reinforces the observation that detached Π structures are not correctly captured by the reconstructed field, probably because their limited wall-normal extent does not produce the necessary footprint at the wall to allow for their reconstruction.

5. Conclusions

We have shown that several properties of the flow in a turbulent channel can be reconstructed to good accuracy from the observation of the pressure and of the two velocity shears at the wall. Because the pressure and the second invariant, Π, of the velocity gradient tensor are linked by a Poisson equation, the latter can be expressed as a projection of the former on a Green's function, and the optimal reconstruction can be posed as an orthogonal projection problem. However, the result of this projection is physically unsatisfactory, and a better strategy is to take into account the statistics of Π, in the form of its two-point autocorrelation function. The resulting procedure is equivalent to linear stochastic estimation, and provides reconstructed Πs which agree very well with the observed ones in the viscous layer, reasonably well below $y^+ \approx 100$, and well for large-scale structures farther from the wall. Correspondingly, only large enough structures far from the wall create a footprint on the wall pressure. The reconstructed Π structures share many characteristics with the attached vortex clusters described by del Álamo *et al.* (2006). This would, at least in principle, allow active control techniques to be performed using only wall observables.

Acknowledgments

Computational resources from the European Research Council (grant# ERC-2014.AdG-669505) are gratefully acknowledged. We are grateful to Prof. Ricardo García-Mayoral for his careful and prompt critique of an early version of the manuscript.

REFERENCES

Adrian, R. J. 1994 Stochastic estimation of conditional structure: a review. *Appl. Sci. Res.* **53**, 291–303.

del Álamo, J. C., Jiménez, J., Zandonade, P. & Moser, R. D. 2006 Self-similar vortex clusters in the logarithmic region. *J. Fluid Mech.* **561**, 329–358.

Chakraborty, P., Balachandar, S. & Adrian, R. J. 2005 On the relationships between local vortex identification schemes. *J. Fluid Mech.* **535**, 189–214.

Choi, H., Moin, P. & Kim, J. 1994 Active turbulence control and drag reduction in wall-bounded flows. *J. Fluid Mech.* **262**, 75–110.

Dong, S., Lozano-Durán, A., Sekimoto, A. & Jiménez, J. 2017 Coherent structures in statistically stationary homogeneous shear turbulence. *J. Fluid Mech.* **816**, 167–208.

Farrell, B. F. & Ioannou, P. J. 1996 Turbulence suppression by active control. *Phys. Fluids* **8**, 1257–1268.

Flores, O. & Jiménez, J. 2010 Hierarchy of minimal flow units in the logarithmic layer. *Phys. Fluids* **22**, 071704.

Jiménez, J. 2013 How linear is wall-bounded turbulence? *Phys. Fluids* **25**, 110814.

Jiménez, J. 2018 Coherent structures in wall-bounded turbulence. *J. Fluid Mech.* **842**, P1.

Jiménez, J. & Hoyas, S. 2008 Turbulent fluctuations above the buffer layer of wall-bounded flows. *J. Fluid Mech.* **611**, 215–236.

Kim, J. 1989 On the structure of pressure fluctuations in simulated turbulent channel flow. *J. Fluid Mech.* **205**, 421–451.

Kravchenko, A., Choi, H. & Moin, P. 1993 On the relation between near-wall streamwise vortices to wall skin friction in turbulent boundary layers. *Phys. Fluids A* **5**, 3007–3009.

Lozano-Durán, A., Flores, O. & Jiménez, J. 2012 The three-dimensional structure of momentum transfer in turbulent channels. *J. Fluid Mech.* **694**, 100–130.

Lozano-Durán, A. & Jiménez, J. 2014 Effect of the computational domain on direct simulations of turbulent channels up to $Re_\tau = 4200$. *Phys. Fluids* **26**, 011702.

Moin, P. & Moser, R. D. 1989 Characteristic-eddy decomposition of turbulence in a channel. *J. Fluid Mech.* **200**, 471–509.

Moisy, F. & Jiménez, J. 2004 Geometry and clustering of intense structures in isotropic turbulence. *J. Fluid Mech.* **513**, 111–133.

Rawlins, F., Ballard, S. P., Bovis, K. J., Clayton, A. M., D.Li, Inverarity, G. W., Lorenc, A. C. & Payne, T. J. 2007 The Met Office global four-dimensional variational data assimilation scheme. *Q. J. R. Meteorol. Soc.* **133**, 347–362.

Sontag, E. D. 1998 *Mathematical Control Theory*. Springer.